

Mass spectrometry imaging of endogenous metabolites in response to doxorubicin in a novel 3D osteosarcoma cell culture model

PALUBECKAITĖ, Ieva, CROOKS, Lucy <<http://orcid.org/0000-0002-3344-8587>>, SMITH, David <<http://orcid.org/0000-0001-5177-8574>>, COLE, Laura <<http://orcid.org/0000-0002-2538-6291>>, BRAM, Heijs, LE MAITRE, Christine <<http://orcid.org/0000-0003-4489-7107>>, CLENCH, Malcolm <<http://orcid.org/0000-0002-0798-831X>> and CROSS, Neil A <<http://orcid.org/0000-0003-2055-5815>>

Available from Sheffield Hallam University Research Archive (SHURA) at:

<https://shura.shu.ac.uk/25359/>

This document is the Accepted Version [AM]

Citation:

PALUBECKAITĖ, Ieva, CROOKS, Lucy, SMITH, David, COLE, Laura, BRAM, Heijs, LE MAITRE, Christine, CLENCH, Malcolm and CROSS, Neil A (2019). Mass spectrometry imaging of endogenous metabolites in response to doxorubicin in a novel 3D osteosarcoma cell culture model. *Journal of Mass Spectrometry*. [Article]

Copyright and re-use policy

See <http://shura.shu.ac.uk/information.html>

1 **Mass spectrometry imaging of endogenous metabolites in response to doxorubicin**
2 **in a novel 3D osteosarcoma cell culture model**

3
4
5
6

Ieva Palubeckaitė¹, Lucy Crooks², David P. Smith², Laura M. Cole², Heijs Bram³,
Christine Le Maitre², Malcolm R. Clench² and Neil A. Cross^{2*}

7 ¹Department of Pathology, Leiden University Medical Center, PO BOX 9600, 2300 RC
8 Leiden, the Netherlands.

9 ²Centre for Mass Spectrometry Imaging, Biomolecular Sciences Research Centre,
10 Sheffield Hallam University, Howard Street, Sheffield S1 1WB

11 ³Center for Proteomics and Metabolomics, Leiden University Medical Center, PO BOX
12 9600, 2300 RC Leiden, the Netherlands.

13
14
15
16
17
18
19
20
21
22
23
24

25 *Corresponding Author: Dr Neil Cross, Centre for Mass Spectrometry Imaging,
26 Biomolecular Sciences Research Centre, Sheffield Hallam University, Howard Street,
27 Sheffield S1 1WB email: n.cross@shu.ac.uk

28

29 **Keywords**

30 Osteosarcoma, 3D cell culture, mass spectrometry imaging, doxorubicin, multivariate
31 analysis.

32 **Abstract**

33 Three-dimensional (3D) cell culture is a rapidly emerging field which mimics some of the
34 physiological conditions of human tissues. In cancer biology, it is considered a useful tool in
35 predicting *in vivo* chemotherapy responses compared with conventional two-dimensional cell
36 culture. We have developed a novel 3D cell culture model of osteosarcoma comprised of
37 aggregated proliferative tumour spheroids, which shows regions of tumour heterogeneity
38 formed by aggregated spheroids of polyclonal tumour cells. Aggregated spheroids show local
39 necrotic and apoptotic regions, and have sizes suitable for the study of spatial distribution of
40 metabolites by mass spectrometry imaging (MSI). We have used this model to perform a
41 proof-of-principle study showing a heterogeneous distribution of endogenous metabolites that
42 co-localise with the necrotic core and apoptotic regions in this model. Cytotoxic
43 chemotherapy (Doxorubicin) responses were significantly attenuated in our 3D cell culture
44 model compared with standard cell culture, as determined by Resazurin assay, despite
45 sufficient doxorubicin diffusion demonstrated by localisation throughout the 3D constructs.
46 Finally, changes to the distribution of endogenous metabolites in response to Doxorubicin
47 were readily detected by MSI. Principle component analysis identified 50 metabolites which
48 differed most in their abundance between treatment groups, and of these, 10 were identified
49 by both in-software *t test* and mixed effects ANOVA. Subsequent independent MSI of
50 identified species were consistent with principle component analysis findings. This proof-of-
51 principle study shows for the first time that chemotherapy-induced changes in metabolite
52 abundance and distribution may be determined in 3D cell culture by MSI, highlighting this
53 method as a potentially useful tool in elucidation of chemotherapy responses as an alternative
54 to *in vivo* testing.

55

56

57

58

59 1 Introduction

60

61 The current process of drug discovery and development, based on standard cell culture *in*
62 *vitro* assays followed immediately by *in vivo* studies has produced many effective drug
63 candidates, however this workflow has limitations. Cells grown in standard or 2-dimensional
64 cultures (2D) do not reflect the environment within tumours, which contain heterogeneous
65 cellular environments, with proliferative, quiescent, apoptotic and necrotic regions resulting
66 from oxygen and nutrient-deprivation. Within tumours, oxygen and nutrient deprivation is in-
67 part due to chaotic vasculature and/or considerable extracellular matrix deposition, leading to
68 impaired drug delivery to tumours. In contrast cells in 2D culture receive optimal oxygen,
69 growth factors, and in the case of therapeutics studies, equal drug concentrations equating to
70 that in the medium. The study of drug distributions and effects on downstream pathways via
71 metabolomics approaches have successfully been used to predict anti-tumour cytotoxic
72 responses by the analysis of extracellular metabolites in cancer patients.¹⁻² These
73 metabolomic studies have been extended to 3-dimensional (3D) cell culture studies, whereby
74 the environment recapitulates the drug resistance seen *in vivo*,³⁻⁴ and have further shown that
75 metabolomic profiles may predict the malignant potential of cells grown in 3D cell culture.⁵

76

77 Numerous 3D cell culture models for the study of drug responses have been developed,
78 however many of these are unsuited to spatial localisation studies due to the small size of
79 resulting cell constructs. Sodium alginate, a naturally occurring polysaccharide extracted
80 from algae, which following chelation with Ca^{2+} , forms cross-links creating a scaffold, and
81 has been used previously for 3D culture of cancerous cells.⁶ This method has the advantage
82 of being a clonal grown model dependent on the colony-forming ability of cancer cells,
83 which is a key characteristic of cancer stem cells or tumour initiating cells.⁷ However, in this
84 model, spheres develop slowly, and few spheres reach over 400 μm diameter, which is
85 insufficient for spatial investigation of molecular distribution by most MSI modalities.⁸

86

87 Multicellular tumour spheroids (MCTS) are formed through use of ultra-low adherence
88 techniques, which allows the generation of larger, uniform spheres through aggregation,
89 rather than proliferation, with the possibility of constructs around 1mm size.⁸ MCTS models
90 show clear hypoxic cores, apoptotic, quiescent and viable regions representative of tumours,

91 and both metabolites and proteins have been successfully imaged within 3D cell cultures by
92 MALDI-MSI.⁹ Furthermore, MALDI-MSI of metabolite distribution is possible, with species
93 localised to viable and hypoxic core regions in MCTS generated in low-adherence wells.¹⁰
94 MALDI-MSI-based metabolite distribution in pellet cultures of chondrocytes show varying
95 spatial distributions in hypoxic vs. normoxic regions, further supported by pellet cultures
96 generated in hypoxic conditions.¹¹ MALDI-MSI has also successfully demonstrated spatial
97 and temporal drug distribution (irinotecan, leucovorin, and its metabolites) in 3D MCTS
98 cultures,¹² and irinotecan distributions in patient-derived organoids.¹³ Although patient-
99 derived ‘organoid’ models better represent patient tumours than cell line models and are in
100 development for sarcoma,¹⁴ these are only well developed for epithelial cancers. Suitable
101 osteosarcoma cell line-based 3D models to allow disease-relevant *in vitro* drug responses,
102 including MSI studies, are required.

103

104 Since many 3D cell culture models such as MCTS are aggregation models, rather than clonal
105 proliferation models, these may not fully recapitulate the heterogeneous nature of tumours.
106 Even within apparently homogeneous established cell lines, heterogeneous populations exist,
107 and adjacent clones of cells may respond differently to the same cytotoxic stimuli.¹⁵ To
108 circumvent these limitations, we have developed an aggregated spheroid model, creating
109 large constructs of ~1mm diameter from isolated, clonal tumour spheres generated from an
110 alginate bead culture. This creates a tissue construct that is a) sufficiently large for spatial
111 distribution studies by MSI, b) contains a necrotic core, apoptotic and viable regions and c)
112 contains intra-tumoural heterogeneity.

113

114 Doxorubicin was chosen to observe drug distribution and identify the metabolomic and
115 lipidomic response of the 3D cell culture. Doxorubicin is an anthracycline which interferes
116 with DNA transcription and replication through the stabilisation of topoisomerase II.
117 Doxorubicin is one of the most widely used drugs for the treatment of high-grade
118 osteosarcoma.¹⁶ In this study, we performed a proof-of-principle study to test whether a
119 heterogeneous metabolite distribution could be detected by MSI, and to image Doxorubicin-
120 induced changes in metabolite changes in response to cytotoxic chemotherapy in 3D cell
121 culture.

122

123 **2 Methods and Materials**

124 **Cell culture**

125 The SAOS-2 osteosarcoma cell line was obtained from American Type Culture Collection
126 (ATCC) and cultured in MEM α (Lonza Ltd, Switzerland) containing 10% foetal bovine
127 serum (FBS) and 10 U/ml penicillin and 10 $\mu\text{g}/\text{mL}$ streptomycin (Thermo Scientific, USA). It
128 was maintained in a humidified atmosphere containing 5% CO_2 at 37°C.

129 **3D cell culture**

130 Following expansion in a monolayer, cell lines were suspended in 1.2% w/v medium
131 viscosity alginate (Sigma-Aldrich, UK) in 0.15M NaCl at 1×10^5 cells/mL. Alginate beads
132 were formed via dropping the cellular suspension in 1.2% w/v alginate/0.15 M NaCl (Sigma-
133 Aldrich, UK) through a 19-gauge needle into 0.2 M CaCl_2 (Sigma-Aldrich, UK). After
134 incubation at 37°C for 12 minutes, alginate beads were washed twice with 0.15 M NaCl and
135 washed twice in complete media before being placed in the appropriate culture media for 28
136 days. To release clonal tumour spheres from the alginate matrix, alginate beads were
137 dissolved in 500 μL dissolving buffer per bead (55 mM sodium citrate (Sigma-Aldrich, UK),
138 30mM EDTA (Sigma-Aldrich, UK), 0.15 M NaCl) for 10 minutes at 37°C with agitation.
139 Following centrifugation, spheroids were immediately placed in 1% agarose-coated (non-
140 adherent) 96 well plates and cultured for a further 7 days.

141

142 **Chemotherapeutic treatment of 2D and 3D cultures**

143 Once confluent, SAOS-2 osteosarcoma cells were trypsinised and seeded into 96-well plates
144 at 5×10^4 cells/mL. These were allowed to adhere for 24 hours before treatment. Cells were
145 treated with 0-12.8 μM Doxorubicin hydrochloride (Sigma-Aldrich, UK), or 0-4 μM for 3D
146 cell culture studies, for up to 48 hours, with treatment media replaced every 24 hours, for 3
147 independent cell culture experiments. To assess cell activity/survival during treatment a
148 Resazurin assay was used. Resazurin (Sigma-Aldrich, UK) stock was made at 3mg/mL in
149 αMEM media. Resazurin diluted in complete media (200 μL of 0.3 mg/mL) was added to
150 each well and incubated for 1.5 hours (2D culture) or 3 hours (3D culture) at 37°C, wrapped
151 in foil to protect from light exposure. The fluorescence was recorded using a 530 nm
152 excitation/590 nm emission filter set using a Clariostar microplate reader (BMG Labtech Ltd,
153 UK). After reading the plates the cultures were washed twice with culture medium and
154 cultured further until the last remaining time point. Additionally, doxorubicin controls were

155 tested in order to confirm the absence of fluorescent interference with the assay. The
156 Resazurin fluorescence values were shown to deviate from the normal distribution by the
157 Shapiro-Wilk test of normality. Therefore, the Kruskal-Wallis test was used to determine if
158 there was a significant difference between Doxorubicin treatments. The Dwass-Steel-
159 Chritchlow-Fligner *post-hoc* test was performed for all pairwise comparisons when a
160 significant difference was observed between treatment groups. When a decrease in cell
161 survival at higher doses was observed, a non-linear regression of (variable) on \log_{10} dose was
162 fit with four parameters in GraphPad Prism (v7) (GraphPad Software, USA).

163

164 **Fluorescent imaging of spheroid aggregates**

165 To visualise drug distribution in spheroid aggregates, cells were treated with 1 μM
166 Doxorubicin for 6 hours then stained for 25 mins with Hoechst 33342 (10 $\mu\text{g}/\text{mL}$). The
167 fluorescence was visualised on an Olympus IX81 microscope with an Olympus XM10
168 camera using Texas Red and DAPI channels respectively and analysed using Olympus
169 Cell[^]F software (Olympus, Germany). Apoptosis was visualised using NucView 488
170 Caspase-3 fluorogenic substrate (Biotium, Cambridge Research, UK) as per manufacturers'
171 instructions, then counterstained with Hoechst 33342 as above. Necrotic regions were
172 identified by staining simultaneously with Propidium Iodide and Hoechst 33342 staining
173 (both 10 $\mu\text{g}/\text{mL}$).

174

175 **MALDI-MSI and detection of Doxorubicin in 3D cell culture**

176 A doxorubicin standard-spiked cell plug array was made to aid detection of doxorubicin
177 inside a spheroid using MALDI-MSI to mimic the signal suppression effects in the samples.
178 A gelatin block was made by pouring 20% w/v gelatin (Sigma-Aldrich, UK) into ice cube
179 moulds, setting the moulds (4°C) for 4 hours, and transferring to -80°C for storage. The block
180 was transferred from -80°C to a -30°C cryostat and the top cut down to produce an even
181 surface. Using a pillar drill, nine 2.5x10mm holes were then drilled into the frozen block
182 which was mounted in a cryostat set to -30°C. SAOS-2 cells were trypsinised, counted,
183 centrifuged and the supernatant removed. A range of doxorubicin concentrations (0, 0.031,
184 0.063, 0.125, 0.25, 0.5, 1, 2, 4 μM) were produced by mixing pelleted cells 2:1 with
185 doxorubicin diluted in culture medium and placing the mixture in each cell plug hole, filling

186 an approximate volume of 49 μ L, and stored in a sealed container in -80°C prior to MALDI-
187 MSI.

188

189 Spheroid aggregates treated with 0, 0.16, 0.8, and 4 μM doxorubicin were harvested at 0 and
190 48 hours and embedded in 5% w/v gelatin + 2.5% carboxymethylcellulose (CMC) (Sigma-
191 Aldrich, UK) inside a silicone mould, immediately frozen using liquid nitrogen and stored in
192 air-tight containers. Sample sections were cut using the Leica 1850 UV cryostat (Leica
193 Biosystems, UK), set to -30°C , at 10 μm thickness, thaw mounted on a positively charged X-
194 tra® adhesive slide (Leica Biosystems, UK) or on an Indium-Tin oxide (ITO)-coated slide
195 (Visiontek Systems Ltd, UK), dependant on the analysis. All sample sections were taken
196 straight after cryosectioning or from -80°C storage and immediately placed in a vacuum
197 desiccator for ~15 minutes prior to matrix application. Negative mode imaging was
198 performed with NEDC (Sigma-Aldrich, UK) (7 mg/mL, 50% MeOH) prepared as a matrix
199 solution. The matrix was applied to the sample section using the SunCollect™ (Sunchrom,
200 Germany) automated sprayer. Fifteen layers of matrix were applied, at 4 $\mu\text{L}/\text{min}$ for the first
201 layer and 3.5 $\mu\text{L}/\text{min}$ for the remaining layers (speed x: low 7, speed y: medium 1, Z position:
202 35).

203

204 Imaging of the Doxorubicin spiked plug array and doxorubicin-treated spheroid aggregates
205 was initially performed in negative mode using an Autoflex III, as it was equipped with a
206 smartbeam laser which proved better for doxorubicin detection and was able to detect small
207 molecules at lower spatial resolution settings. Negative ion mass spectra were acquired at a
208 pixel size of 30 μm from m/z 50 – m/z 1000 in reflectron mode. The laser was focused to
209 around 30 μm diameter. Four hundred laser shots were acquired for each spectrum. Data
210 acquisition was performed using FlexControl (Bruker Daltonics, Germany), and
211 visualizations were obtained from FlexImaging 4.0 (Bruker Daltonics, Germany).

212

213 **MALDI-MSI of Doxorubicin-induced changes to endogenous metabolites in 3D cell** 214 **culture**

215 Treated spheroid aggregates (0, 0.8, 4 μM) were sectioned as before at 10 μm thickness,
216 ensuring a section from the middle part of the spheroid aggregate was sampled. Three
217 independent culture experiments were performed, and from each culture, three aggregated

218 spheroids were used, and three sections taken from each aggregated spheroid resulted in a
219 total of 81 sections for MSI. The NEDC matrix deposition protocol used was as above.

220

221 Imaging of metabolite changes in response to Doxorubicin in spheroid aggregates was
222 executed using a Synapt G2 (Waters, UK) in sensitivity mode as this instrument was capable
223 of sufficient mass resolution and high enough throughput for the large sample comparison.
224 Images of 60µm pixel size were acquired. Data was acquired over an m/z range of 50–1,000
225 in negative mode analysis. For positive mode imaging of doxorubicin inside a spheroid
226 aggregate, images of 60µm were acquired at m/z 100-1200. The ion mobility function was
227 used to improve separation of peaks. Data acquisition and analysis was performed using
228 MassLynx v4.1 (Waters, UK) and High Definition Imaging (HDI) Software (Waters, UK).
229 Tandem MS fragmentation was performed using an isolation window of 0.3 Da.

230

231 Regions of interest (ROIs) containing whole spheroid aggregates were selected in Waters
232 HDI 1.4 imaging software and exported as average spectra into MassLynx software. They
233 were then centroided and exported as .txt files and imported into Marker View software 1.2
234 (Applied Biosystems/MDS Sciex, Canada). An exclusion list to remove NEDC peaks was
235 applied to the datasets, to remove the influences of the matrix signals when observing
236 relationships of the treatment groups between spectra. The data were restricted to 5000 peaks
237 and 0.1 minimum intensity and autoscaled. Principal Component Analysis-Discriminant
238 Analysis (PCA-DA) was used to demonstrate that the spectral data could be used to visually
239 discriminate between doses, and performed by informing the MarkerView software which
240 samples belonged to each treatment group. The software then selected the two components
241 that explained the most variance in normalised signal intensity over the peaks between
242 groups.

243

244 Initially, a pragmatic approach was taken to analysing the data, aimed at balancing statistical
245 rigour against time requirements for such high dimensional data with the software being used.
246 Reduced Synapt data generated by the PCA-DA was initially put through a screening by *t test*
247 comparison of each treatment group against each other. Potential effects of batch, culture and
248 slice were ignored. The 50 peaks with lowest *P*-values for any comparison were then
249 analysed further. The normalised signal intensities significantly deviated from the normal

250 distribution by Shapiro-Wilk tests. Therefore, Kruskal-Wallis tests were applied to each ionic
251 species to determine if there was a significant effect of dose. This analysis was combined
252 with Dwass-Steel-Christchlow-Fligner *post-hoc* test when a significant difference was seen
253 between treatment groups. Statistical analysis was performed using StatsDirect software
254 (StatsDirectLtd, UK).

255

256 The inclusion of different batches, cultures and slices enables the variation due to these
257 factors to be estimated and accounted for in statistical modelling, which increases the power
258 to detect any dose effects. The data were exported from MarkerView R (v 3.4.1).¹⁷ R is
259 programmable software that enables a statistical test to be automated for very large numbers
260 of variables. A linear mixed effect model was fit by restricted maximum likelihood for the
261 normalised signal intensity of each peak using the function lme in package nlme (v 3.1-
262 131)¹⁸. Batch and culture nested within batch were fitted as random effects and dose as a
263 fixed effect¹⁸. An effect of dose was tested with an F test by applying the anova function to
264 the fitted model object. The significance threshold was set to $P=1 \times 10^{-5}$, which is a Bonferroni
265 correction of $P=0.05$. Where a significant effect of dose was found, the model was re-run
266 with the ordering of the levels of dose changed, to obtain P values from t tests of each
267 pairwise comparison. The residuals from the model were also plotted against the fitted values
268 to check they met the assumptions of a parametric analysis.

269 The significantly differing peaks discovered using either statistical approach were given
270 putative assignments based on a database search in the Human Metabolome, Metlin or
271 LipidMaps search databases. The error allowance used was 30ppm for small molecules and
272 0.01 Da for lipid identifications which was acceptable for the data acquired. Following the
273 database search biological relevance was investigated within the possible identities within
274 current literature.

275

276 **Confirmation of Doxorubicin-induced metabolite changes by Fourier-Transform Ion** 277 **Cyclotron Resonance (FT-ICR) MSI**

278 To confirm the findings from the PCA study MALDI-FTICR-MSI of 0, 0.8 and 4 μ M
279 doxorubicin-treated spheroid aggregates was performed on a 9.4T SolariX XR mass
280 spectrometer (Bruker Daltonics, Germany) in negative-ion mode, using 200 laser shots per
281 spot and 75 μ m pixel size. Data was acquired in a m/z range from 50 to 1000 Da. For positive

282 mode imaging of doxorubicin inside a spheroid aggregate, 220 laser shots were used per spot
283 at a 75 μ m pixel size. Data was acquired at m/z 100-1200. Data acquisition was performed
284 using ftmsControl (Bruker Daltonics, Germany), and visualizations were obtained from
285 flexImaging4.0 (Bruker Daltonics, Germany). As this instrument has a higher mass resolving
286 power, both doxorubicin and the endogenous small molecules were clearer, however the
287 method was only used to confirm due to large data sizes and analysis time requirements. The
288 previously determined putative identifications were confirmed with the FTICR analysis
289 within 3 ppm.

290

291

292 **3 Results and discussion**

293 **Development of the SAOS-2 aggregated spheroid model**

294 The SAOS-2 spheroid aggregate model was developed to allow sufficient spatial resolution
295 of metabolites by MSI. Initial growth of SAOS-2 in alginate resulted in colonies typically
296 200 μM diameter, which may not provide sufficient information in low spatial resolution
297 imaging experiments. To circumvent this problem, whilst keeping the presence of clonal
298 heterogeneity, the alginate matrix was dissolved to release clonal tumour spheroids, which
299 were subsequently aggregated in low-adhesion agarose-coated wells (Fig 1a). This process
300 resulted in constructs of up to 1 mm. Staining of aggregated spheroids with Hoechst 33342,
301 to localise all cells (blue), and propidium iodide, to localise regions containing necrotic cells
302 (red) revealed heterogeneity across the tissue construct, with a clear viable rim containing no
303 necrotic cells (Fig 1b). Caspase-3 is one of the executioner caspases at the end of the
304 apoptotic cascade, and active caspase-3 is characteristic of apoptotic cell death and is present
305 in regions of hypoxia in 3D cell cultures.¹⁹ Staining for Caspase-3 activity using the
306 NucView 488 fluorogenic Caspase-3 substrate revealed heterogeneous regions of apoptosis
307 localised to the centre of the construct, whilst the viable rim remained devoid of active
308 caspase-3. These results highlight the heterogeneous nature of aggregated spheroids, which
309 contrasts with more uniform constructs generated from hanging-drop or aggregation of cell
310 suspensions in low-adhesion plates.

311

312 **Spatial distribution of endogenous metabolites within aggregated spheroids**

313 MALDI-MSI of tumour spheroids revealed regional variations within the aggregated
314 spheroids (Fig 2). Phosphoric acid (m/z 78.9493) was used to localise the aggregated spheroid
315 construct. Detection of peaks with considerable variation in spatial distribution within the
316 spheroid is evident, with m/z 426.0657 showing focal regions of detection, and m/z 281.2809
317 absent in the centre, and also at the periphery whereas localisation of m/z 403.1034 can be
318 seen to localise within the central necrotic core region. Both m/z 158.9409 and m/z 606.0975
319 are largely absent from the viable rim region, with the latter showing evidence of
320 delocalisation beyond the cellular construct, along with phosphoric acid.

321

322 **SAOS-2 cells respond to doxorubicin, but not in 3D cell culture**

323 Treatment of SAOS-2 cells with doxorubicin displayed a dose-dependent and time-dependent
324 decrease in cell activity in 2D cell culture. Cell activity was reduced at 36 hours treatment
325 compared to 12 hrs ($p < 0.0001$) with an IC_{50} of $1.09 \mu M$ after 36 hours (Fig 3a). In contrast,
326 treatment of 3D aggregated spheroids resulted in no significant reduction of cell viability at
327 doses up to $4 \mu M$ after 48 hours (Fig 3b). Impaired response to Doxorubicin in 3D cell
328 culture is not unexpected, and hypoxia-induced resistance to doxorubicin has been reported in
329 similar models.²⁰⁻²¹ It is well known that the central regions of MCTS are acutely hypoxic,
330 resulting in apoptosis and necrosis,²² which is consistent with observations seen in this
331 model, and therefore likely accounting for observed lack of cytotoxic effects in this study.

332

333 To confirm Doxorubicin penetration into the 3D aggregated spheroid constructs, Doxorubicin
334 distribution was determined by fluorescence microscopy. Since Doxorubicin fluoresces, drug
335 distribution can easily be seen throughout the aggregated spheroid (red), as compared to
336 Hoechst 33342 counterstain, which enters all cells (blue) (Fig 3c). After just 6 hours, $1 \mu M$
337 doxorubicin can clearly be seen staining cells within the spheroid aggregate, whereas post-
338 staining with Hoechst 33342 shows only staining of the outer layer of cells, consistent with
339 previous observations of Doxorubicin uptake in MCTS models.²³

340

341 Cell plug arrays were made to aid detection of doxorubicin inside the spheroid aggregates.
342 This was made by mixing SAOS-2 cells with doxorubicin standard and spiking these cells
343 into a gelatin block. These could then be sectioned alongside the sample of interest and used
344 as an internal standard array to demonstrate qualitative changes to doxorubicin within the
345 sample (Fig 3).

346

347 Initial detection of Doxorubicin within the cell plug arrays was unsuccessful in positive mode
348 by Q-TOF MS due to a close, interfering lipid peak (Fig 3d). The close interference within
349 the spheroid aggregates was not significant at higher doxorubicin concentrations but once at a
350 biologically relevant level, it was substantial. To achieve detection, alternative instrument
351 types (FT-ICR) and negative mode were used enable visualisations. Putative doxorubicin
352 could be observed in negative mode showing a promising increase in signal concurrent with
353 an increase in doxorubicin signal intensity (Fig 3e).

354

355 **Detection of endogenous metabolite changes in response to doxorubicin by MSI**

356 In order to define the metabolomic and lipidomic spheroid aggregate response to
357 Doxorubicin, 48-hour Doxorubicin-treated, and untreated spheroid aggregate sections were
358 imaged in negative mode. The whole spheroid region was selected, and average spectra were
359 extracted for comparison between groups. Comparison was performed using PCA-DA, which
360 takes into account the group the sample belongs to and finds the principle components which
361 separate these groups. The control and treatment groups were separated, and several species
362 were separated out in the loading plot, in particular the 4 μ M treatment group (Fig 4).

363

364 **Linear mixed effects analysis**

365 The approach of using a combination of *t* tests within the MarkerView software to identify 50
366 peaks for follow-up testing by a Kruskal-Wallis test, found a significant effect of dose on the
367 normalised signal intensity of 42 species. Some species were discarded as they were
368 determined to be likely isotopes of other species. Linear mixed effects modelling, which
369 accounts for variation due to batch and culture effects, found 24 species where the normalised
370 signal intensity was significantly altered by dose. Of these, 18 were considered to be unique
371 species (Table 1). Fitting linear mixed models also allowed the random variation in
372 normalised signal intensity due to effects of batch and culture nested within batch, to be
373 estimated. In several cases, one of these variances was negligible, and they were always
374 smaller than the variation amongst slices. Theoretical accurate masses, measured masses and
375 mass errors in ppm for the putative assignments are shown in Table 2. The assigned species
376 were also confirmed within the FTICR imaging data. Ten ionic species (highlighted in Table
377 1) were detected as significant by both methods, which may be indicative of the strong
378 significance of these ionic species in drug response. Results for 6 of these species based on
379 intensities of the whole spheroid area are shown in fig 5. S-nitrosoglutathione (*m/z* 335.0617)
380 (15 ppm) is known to modulate doxorubicin responses in breast cancer cells, whereby N-
381 nitrosoglutathione suppressed doxorubicin activity.²⁴ N-nitrosylation, for which N-
382 nitrosoglutathione is a mediator, is a key step in regulating DNA repair,²⁵ and observed
383 changes likely reflect a DNA damage response. This molecule has been also been shown to
384 induce increased expression of stress response genes and proteins.²⁶
385 Putative identification of *m/z* 378.0869 (28ppm) as S-Lactoylglutathione, which was
386 significantly increased in response to Doxorubicin, is of potential interest to the study of

387 osteosarcoma drug resistance. S-Lactoylglutathione is a known product of the Glyoxalase I
388 (GLO1) enzyme, and is converted to D-lactate regenerating glutathione (Gillespie, 1978)²⁷. A
389 highly significant increase in ionic species m/z 396.0996 was also found. This was putatively
390 identified as S-Adenosyl-4-methylthio-2-oxobutanoate (3ppm) a factor of the modified
391 methionine salvage pathway from 5'-methylthioadenosine (MTA) which could be of interest
392 in cancer as a regulator of apoptosis and proliferation.²⁸ The lipids m/z 714.5375, putatively
393 identified as PE(O-35:2) (0.0068Da); m/z 758.4969, identified as PS(34:2) (0.0009Da); m/z
394 765.5488, identified as PA(41:4) (0.0048Da); m/z 791.5778, and identified as PG(37:0)
395 (0.0030Da) are not directly associated with any known osteosarcoma pathways or
396 doxorubicin responses. However, m/z 765.5488 showed a striking decrease and may be
397 worthy of investigating as a possible marker of drug response.

398

399 MALDI-MSI (FT-ICR-MS) performed in negative mode aimed to validate changes in
400 endogenous metabolites post-Doxorubicin treatment. Metabolomic species were originally
401 acquired using the Synapt G2 and modelled by PCA-DA. Selected ionic species either
402 identified as most highly significantly altered by Doxorubicin treatment, or species with
403 putative identifications with potential relevance to cytotoxic drug responses. MSI is shown in
404 Fig 6, and m/z 355.0617 is shown for comparison as it localised to the entire spheroid
405 aggregate across all treatments. Highly consistent with PCA-DA findings (Fig 5), m/z
406 335.0617, putatively identified as S-nitrosoglutathione showed clear increase, as did m/z
407 378.0869 and m/z 396.0996 putatively identified as S-Lactoylglutathione and S-Adenosyl-4-
408 methylthio-2-oxobutanoate respectively. Doxorubicin (m/z 542.1668) was identified within
409 the same imaging experiment in negative mode, which increased in a dose-dependent manner
410 with treatment, however was only readily detected in the centre of the spheroid where
411 propidium iodide staining was typically observed. This may reflect an ability for Doxorubicin
412 to ionise in intact *vs.* fragmented chromatin of necrotic and apoptotic cells. Ion species m/z
413 714.5375, 765.5488 and 791.5778 were all shown to be decreased by PCA-DA analysis, and
414 subsequent FT-ICR MSI showed presence of all three putative lipids but with signals
415 localised to the centre of the spheroid aggregates. Overall, these data show consistency with
416 PCA-DA analysis of data obtained using Q-TOF and subsequent FT-ICR MSI imaging.

417

418 **Concluding comments**

419 In this study, we have developed a novel 3D cell culture model for osteosarcoma with cell
420 constructs of sufficient size for spatial distribution of endogenous metabolites, and the ability
421 to visualise heterogeneous metabolite distribution within the 3D constructs. We have
422 demonstrated that within these constructs, we can visualise Doxorubicin, and despite the
423 apparent lack of cytotoxic activity of Doxorubicin in 3D cell constructs *vs.* 2D cell culture,
424 metabolomic changes can be imaged and identified using PCA-DA. As further validation of
425 the species identified by PCA-DA analysis of Doxorubicin-treated spheroid aggregates,
426 spatial distribution of changes of some of the most highly significantly altered metabolites
427 followed similar patterns when independently analysed by FT-ICR. Some of the most highly
428 significantly up-regulated species were putatively identified as metabolites of the glutathione
429 system, and agents that modulate the glutathione system are known to modulate Doxorubicin
430 activity.²⁹ In conclusion, MSI of drug-treated 3D cell cultures may identify biologically
431 relevant metabolite changes highlighting this workflow as a potentially useful tool in *in vitro*
432 drug discovery studies.

433 **References**

434 [1] S. Wei, L. Liu, J. Zhang, J. Bowers, G.A. Gowda, H. Seeger, T. Fehm, H.J. Neubauer, U.
435 Vogel, S.E. Clare, D. Raftery. Metabolomics approach for predicting response to neoadjuvant
436 chemotherapy for breast cancer. *Mol Oncol.* **2013** 7, 297-307. doi:
437 10.1016/j.molonc.2012.10.003.

438
439 [2] H. Jia, X. Shen, Y. Guan, M. Xu, J. Tu, M. Mo, L. Xie, J. Yuan, Z. Zhang, S. Cai, J. Zhu,
440 Z. Zhu. Predicting the pathological response to neoadjuvant chemoradiation using untargeted
441 metabolomics in locally advanced rectal cancer. *Radiother Oncol.* **2018** 128, 548-556. doi:
442 10.1016/j.radonc.2018.06.022.

443
444 [3] C. Bingel, E. Koeneke, J. Ridinger, A. Bittmann, M. Sill, H. Peterziel, J.K. Wrobel, I.
445 Rettig, T. Milde, U. Fernekorn, F. Weise, A. Schober, O. Witt, I. Oehme. Three-dimensional
446 tumor cell growth stimulates autophagic flux and recapitulates chemotherapy resistance. *Cell*
447 *Death Dis.* **2017** 8, e3013. doi: 10.1038/cddis.2017.398.

448
449 [4] T.W. Fan, S.S. El-Amouri, J.K.A. Macedo, Q.J. Wang, H. Song, T. Cassel,
450 A.N. Lane. Stable Isotope-Resolved Metabolomics Shows Metabolic Resistance to Anti-
451 Cancer Selenite in 3D Spheroids versus 2D Cell Cultures. *Metabolites.* **2018** 8, pii: E40. doi:
452 10.3390/metabo8030040.

453
454 [5] N. Vidavsky, J.A.M.R. Kunitake, M.E. Diaz-Rubio, A.E. Chiou, H.C. Loh, S. Zhang, A.
455 Masic, C. Fischbach, L.A. Estroff. Mapping and Profiling Lipid Distribution in a 3D Model
456 of Breast Cancer Progression. *ACS Cent Sci.* **2019** 5, 768-780. doi:
457 10.1021/acscentsci.8b00932.

458
459 [6] S.F. Lan, B. Starly. Alginate based 3D hydrogels as an in vitro co-culture model platform
460 for the toxicity screening of new chemical entities. *Toxicol Appl Pharmacol.* **2011** 256, 62-
461 72. doi: 10.1016/j.taap.2011.07.013.

462
463 [7] C. Liu, Y. Liu, X.X. Xu, H. Wu, H.G. Xie, L. Chen, T. Lu, L. Yang, X. Guo, G.W. Sun,
464 W. Wang, X.J. Ma, X He. Potential effect of matrix stiffness on the enrichment of tumor

465 initiating cells under three-dimensional culture conditions. *Exp Cell Res.* **2015** 330, 123-34.
466 doi: 10.1016/j.yexcr.2014.07.036.
467
468
469 [8] A. De Luca, L. Raimondi, F. Salamanna, V. Carina, V. Costa, D. Bellavia, R. Alessandro,
470 M. Fini, G. Giavaresi. Relevance of 3d culture systems to study osteosarcoma environment. *J*
471 *Exp Clin Cancer Res.* **2018** 37, 2. doi: 10.1186/s13046-017-0663-5.
472
473 [9] D.R. Ahlf Wheatcraft, X. Liu, A.B. Hummon. Sample preparation strategies for mass
474 spectrometry imaging of 3D cell culture models. *J Vis Exp.* **2014** 5, 94. doi: 10.3791/52313.
475
476 [10] D.R. Ahlf, R.N. Masyuko, A.B. Hummon, P.W. Bohn. Correlated mass spectrometry
477 imaging and confocal Raman microscopy for studies of three-dimensional cell culture
478 sections. *Analyst.* **2014** 139, 4578-85. doi: 10.1039/c4an00826j.
479
480 [11] B. Bakker, G.B. Eijkel, R.M.A. Heeren, M. Karperien, J.N. Post, B. Cillero-Pastor.
481 Oxygen-Dependent Lipid Profiles of Three-Dimensional Cultured Human Chondrocytes
482 Revealed by MALDI-MSI. *Anal Chem.* **2017** 89, 9438-9444. doi:
483 10.1021/acs.analchem.7b02265.
484
485 [12] X. Liu, A.B. Hummon. Mass spectrometry imaging of therapeutics from animal models
486 to three-dimensional cell cultures. *Anal Chem.* **2015** 87, 9508-19. doi:
487 10.1021/acs.analchem.5b00419.
488
489 [13] X. Liu, C. Flinders, S.M. Mumenthaler, A.B. Hummon. MALDI Mass Spectrometry
490 Imaging for Evaluation of Therapeutics in Colorectal Tumor Organoids. *J Am Soc Mass*
491 *Spectrom.* **2018** 29, 516-526. doi: 10.1007/s13361-017-1851-4.
492
493 [14] M. Gaebler, A. Silvestri, J. Haybaeck, P. Reichardt, C.D. Lowery, L.F. Stancato, G.
494 Zybarth, C.R.A. Regenbrecht. Three-Dimensional Patient-Derived In Vitro Sarcoma Models:
495 Promising Tools for Improving Clinical Tumor Management. *Front Oncol.* **2017** 11, 203.
496 doi: 10.3389/fonc.2017.00203.

497
498 [15] N.A. Cross, E.A. Waterman, N. Jokonya, A. Fowles, C.H. Buckle, J. Phillips, I. Holen,
499 F.C. Hamdy, C.L. Eaton. Phenotypic variations of TRAIL sensitivity in cloned populations of
500 prostate cancer cells. *J Cell Biochem.* **2008** 104, 1452-64. doi: 10.1002/jcb.21721.
501
502 [16] C.M. Hattinger, M. Pasello, S. Ferrari, P. Picci, M. Serra. (2010). Emerging Drugs for
503 High-Grade Osteosarcoma. *Expert Opin. Emerg. Drugs.* **2010** 15, 615–634.
504
505 [17] R Development Core Team (2008). R: A language and environment for statistical
506 computing. R Foundation for Statistical Computing, Vienna, Austria. ISBN 3-900051-07-0,
507 URL <http://www.R-project.org>.
508
509 [18] J. Pinheiro, D. Bates, S. DebRoy, D., Sarkar, R Core Team (2019). nlme: Linear and
510 Nonlinear Mixed Effects Models. R package version 3.1-140, [https://CRAN.R-](https://CRAN.R-project.org/package=nlm)
511 [project.org/package=nlm](https://CRAN.R-project.org/package=nlm)
512
513 [19] S. Kessel, S. Cribbes, S. Bonasu, W. Rice, J. Qiu, L.L. Chan. Real-time viability and
514 apoptosis kinetic detection method of 3D multicellular tumor spheroids using the Celigo
515 Image Cytometer. *Cytometry A.* **2017** 91, 883-892. doi: 10.1002/cyto.a.23143.
516
517 [20] X. Song, X. Liu, W. Chi, Y. Liu, L. Wei, X. Wang, J. Yu. Hypoxia-induced resistance to
518 cisplatin and doxorubicin in non-small cell lung cancer is inhibited by silencing of HIF-
519 1alpha gene. *Cancer Chemother Pharmacol.* **2006** 58, 776-84.
520
521 [21] Y. Imamura, T. Mukohara, Y. Shimono, Y. Funakoshi, N. Chayahara, M. Toyoda, N.
522 Kiyota, S. Takao, S. Kono, T. Nakatsura, H. Minami. Comparison of 2D- and 3D-culture
523 models as drug-testing platforms in breast cancer. *Oncol Rep.* **2015** 33, 1837-43. doi:
524 10.3892/or.2015.3767.
525
526 [22] C.R. Thoma, M. Zimmermann, I. Agarkova, J.M. Kelm, W. Krek. 3D cell culture
527 systems modeling tumor growth determinants in cancer target discovery. *Adv Drug Deliv*
528 *Rev.* **2014** 69-70, 29-41. doi: 10.1016/j.addr.2014.03.001.

529
530
531
532
533
534
535
536
537
538
539
540
541
542
543
544
545
546
547
548
549
550
551
552
553
554
555
556
557
558
559
560

[23] J.K. Lukowski, E.M. Weaver, A.B. Hummon. Analyzing Liposomal Drug Delivery Systems in Three-Dimensional Cell Culture Models Using MALDI Imaging Mass Spectrometry. *Anal Chem.* **2017** 89, 8453-8458. doi: 10.1021/acs.analchem.7b02006.

[24] A. de Luca, N. Moroni, A. Serafino, A. Primavera, A. Pastore, J.Z. Pedersen, R. Petruzzelli, M.G. Farrace, P. Pierimarchi, G. Moroni, G. Federici, P. Sinibaldi, Vallebona, M. Lo Bello. Treatment of doxorubicin-resistant MCF7/Dx cells with nitric oxide causes histone glutathionylation and reversal of drug resistance. *Biochem J.* **2011** 440, 175-83. doi: 10.1042/BJ20111333.

[25] C.H. Tang, W. Wei, L. Liu. Regulation of DNA repair by S-nitrosylation. *Biochim Biophys Acta.* **2012** 1820, 730-5. doi: 10.1016/j.bbagen.2011.04.014.

[26] K.A. Broniowska, A.R. Diers, N. Hogg. S-nitrosoglutathione. *Biochim Biophys Acta.* **2013** 1830, 3173-81. doi:10.1016/j.bbagen.2013.02.004.

[27] E. Gillespie, Concanavalin A increases glyoxalase enzyme activities in polymorphonuclear leukocytes and lymphocytes. *J Immunol.* **1978** 121, 923-5.

[28] E. Albers. Metabolic Characteristics and Importance of the Universal Methionine Salvage Pathway Recycling Methionine from 5'-Methylthioadenosine. *IUBMB Life.* **2009** 61, 1132–1142.

[29] A.A. Mahbub, C.L. Le Maitre, S.L. Haywood-Small, N.A. Cross, N. Jordan-Mahy. Glutathione is key to the synergistic enhancement of doxorubicin and etoposide by polyphenols in leukaemia cell lines. *Cell Death Dis.* **2015** 31;6:e2028. doi: 10.1038/cddis.2015.379.

Ionic species (m/z)	<i>P</i> value	Putative identification
180.4920	4.57x10 ⁻⁶	
245.0544*	1.68x10 ⁻⁷	
253.2270	9.89x10 ⁻⁶	
331.0550*	3.48x10 ⁻¹¹	
335.0617*	<1.00x10 ⁻¹²	S-nitrosoglutathione
347.0637*	1.14x10 ⁻⁷	
364.0735	1.49x10 ⁻⁹	2-S-glutathionyl acetate
378.0869*	2.62x10 ⁻¹¹	S-lactoylglutathione
396.0996*	<1.00x10 ⁻¹²	S-Adenosyl-4-methylthio-2-oxobutanoate
404.0321	1.61x10 ⁻⁷	
414.1022*	<1.00x10 ⁻¹²	
464.0080	1.29x10 ⁻⁶	
565.9493	1.05x10 ⁻⁶	
583.9583	5.98x10 ⁻⁶	
589.9554*	1.92x10 ⁻⁷	
714.5375	9.77x10 ⁻⁸	PE (O-35:2)
765.5488*	1.25x10 ⁻¹⁰	PA (41:4)
791.5778*	3.10x10 ⁻⁷	PG (37:0)

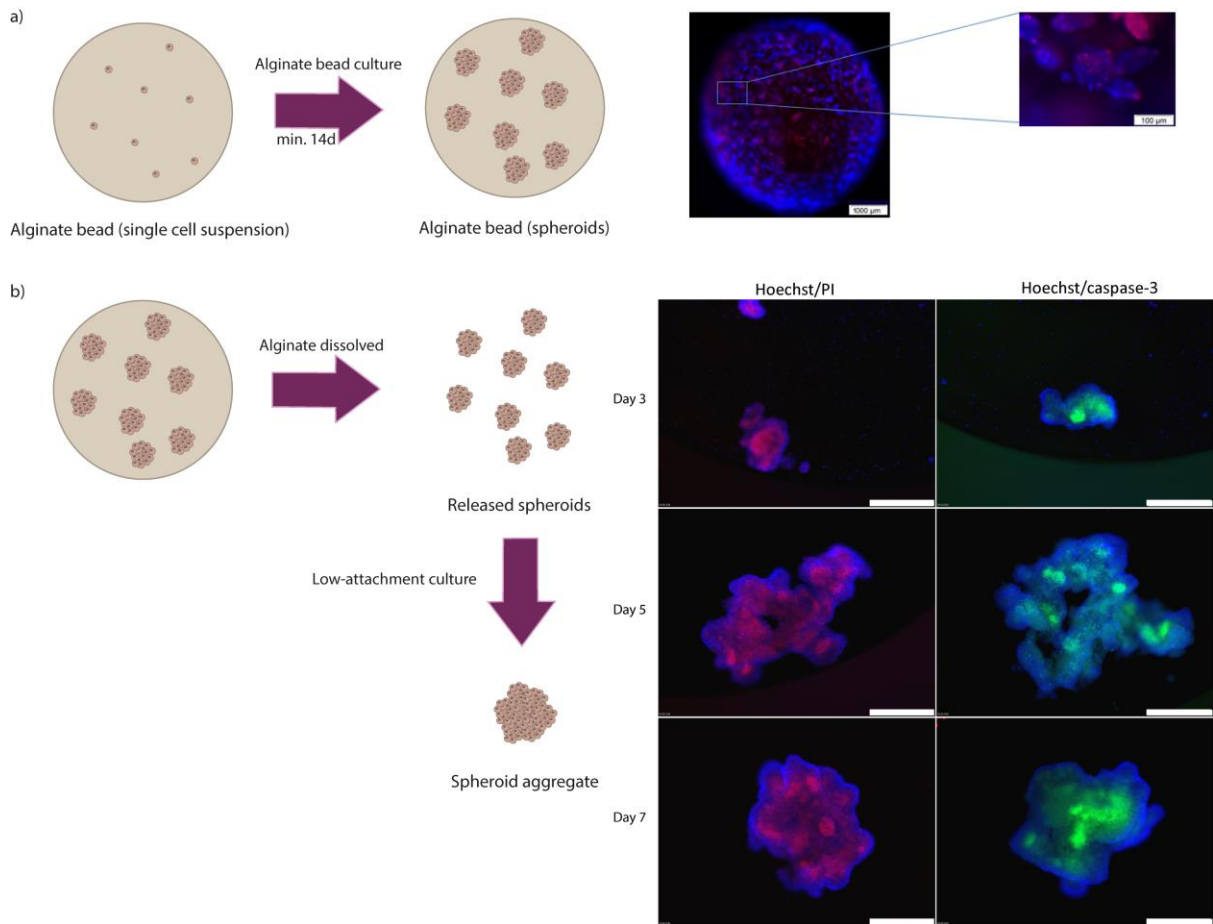
561

562 *Table 1: Ionic species with a significant effect of dose on normalised signal intensity as tested*
563 *by a mixed effects model. The significance threshold was set to $P < 1 \times 10^{-5}$. * indicates species*
564 *that were also identified by the combination of t test and Kruskal-Wallis test.*

Experimental mass (m/z)	Theoretical mass (m/z)	Mass error (ppm)	Assignment
335.0617	335.0667	15	S-nitrosoglutathione
364.0735	364.0820	23	2-S-glutathionyl acetate
378.0869	378.0977	28	S-lactoylglutathione
396.0996	396.0983	3	S-Adenosyl-4-methylthio-2-oxobutanoate
714.5375	714.5443	10	PE (O-35:2)
765.5488	765.5440	6	PA (41:4)
791.5778	791.5808	4	PG (37:0)
858.8311	858.8284	3	1-O-behenoyl-Cer(d34:1)

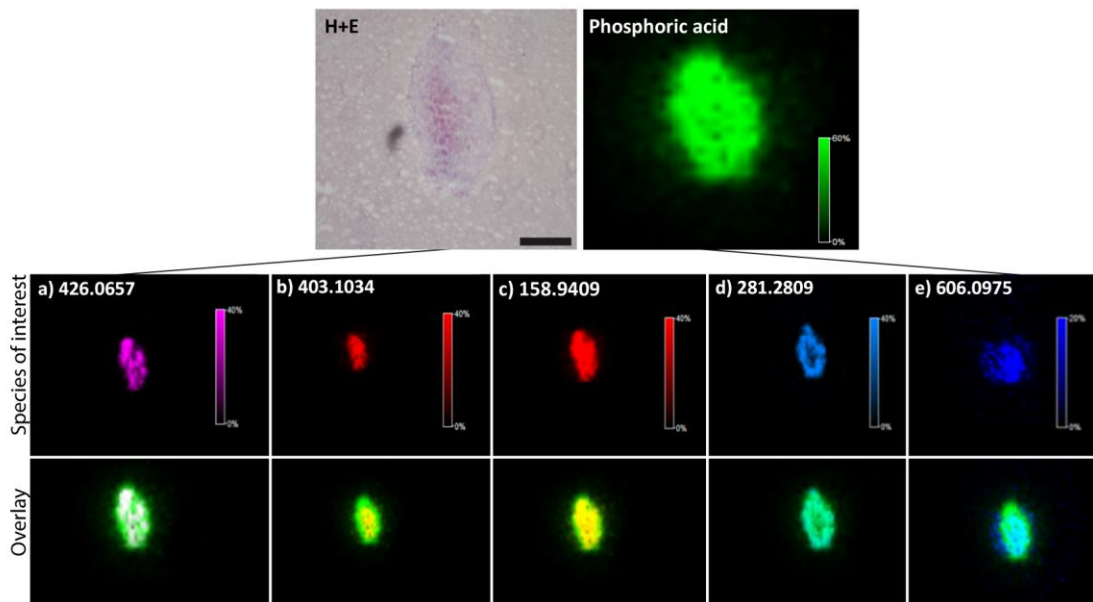
565

566 *Table 2: Theoretical accurate masses, measured masses and mass errors in ppm for the*
567 *putative assignments.*



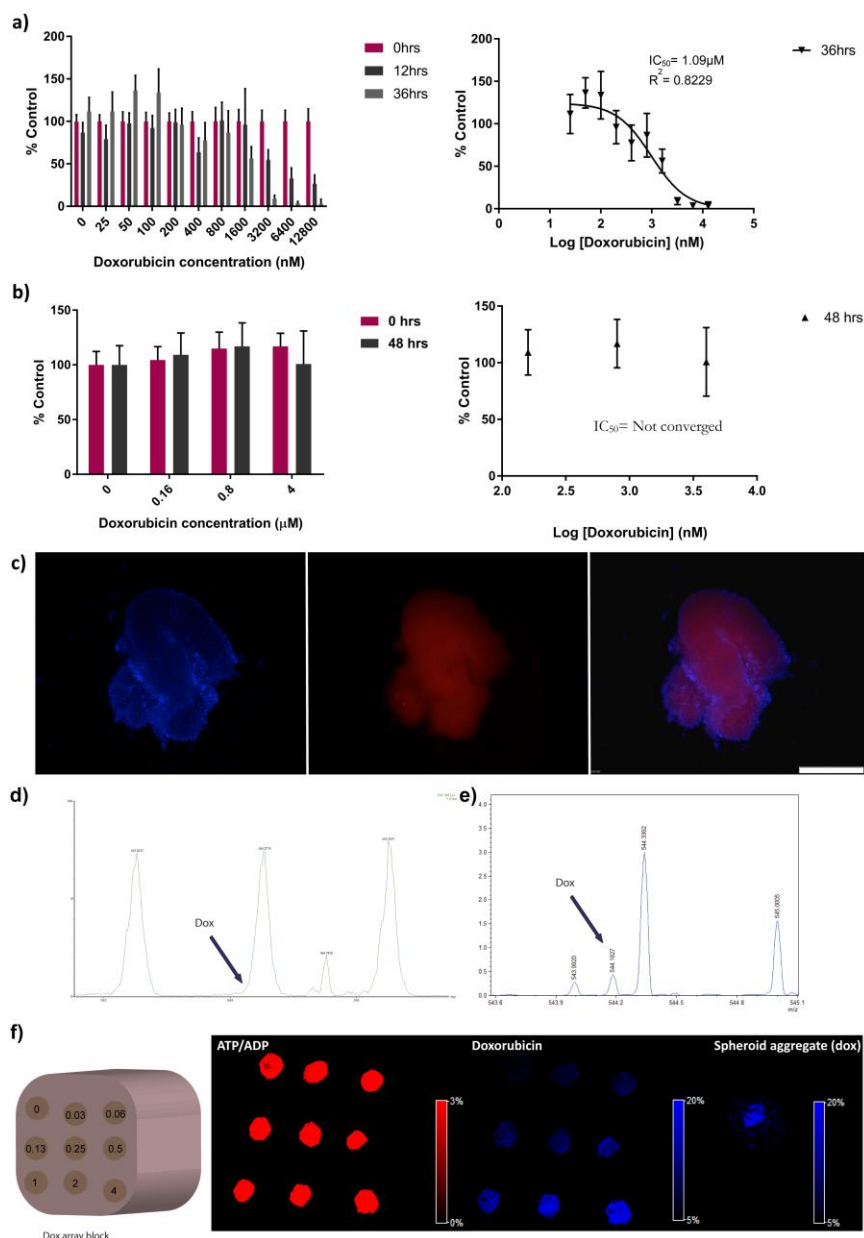
568
 569
 570
 571
 572
 573
 574
 575
 576
 577
 578
 579

Figure 1: Generation of aggregated spheroid model. a) Cells are suspended in alginate and clonal proliferative colonies form. Hoechst 33342 identified all cells and Propidium Iodide identifies regions containing dead cells. b) After alginate dissolution, spheroids are aggregated in a low-adhesion well. Hoechst 33342 and Propidium iodide staining highlights a viable rim with necrotic or dead cells present within the construct, co-localised with caspase-3 activity confirming presence of apoptotic cells within the core. Scale bar=500 µm.



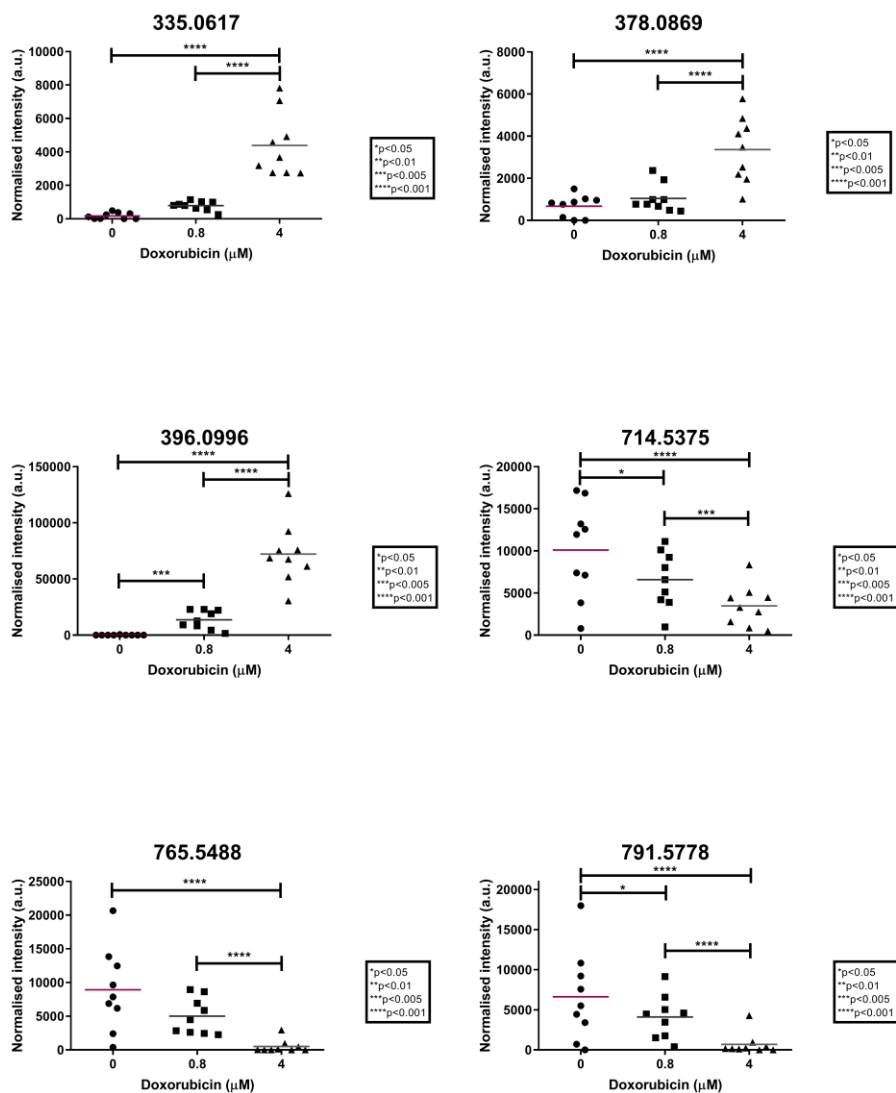
580
 581
 582
 583
 584
 585
 586
 587
 588
 589
 590
 591
 592

Figure 2: Detection and localisation of endogenous metabolites aggregated spheroid model by MSI using Bruker Autoflex III. Haematoxylin and Eosin staining shows the outline of the aggregated spheroid (scale bar = 500 μ M). Phosphoric acid (m/z 78.9493) is ubiquitously present and outlines the aggregated spheroid by MSI. Overlay of phosphoric acid and endogenous metabolites shows heterogeneity of detection within the aggregated spheroid.



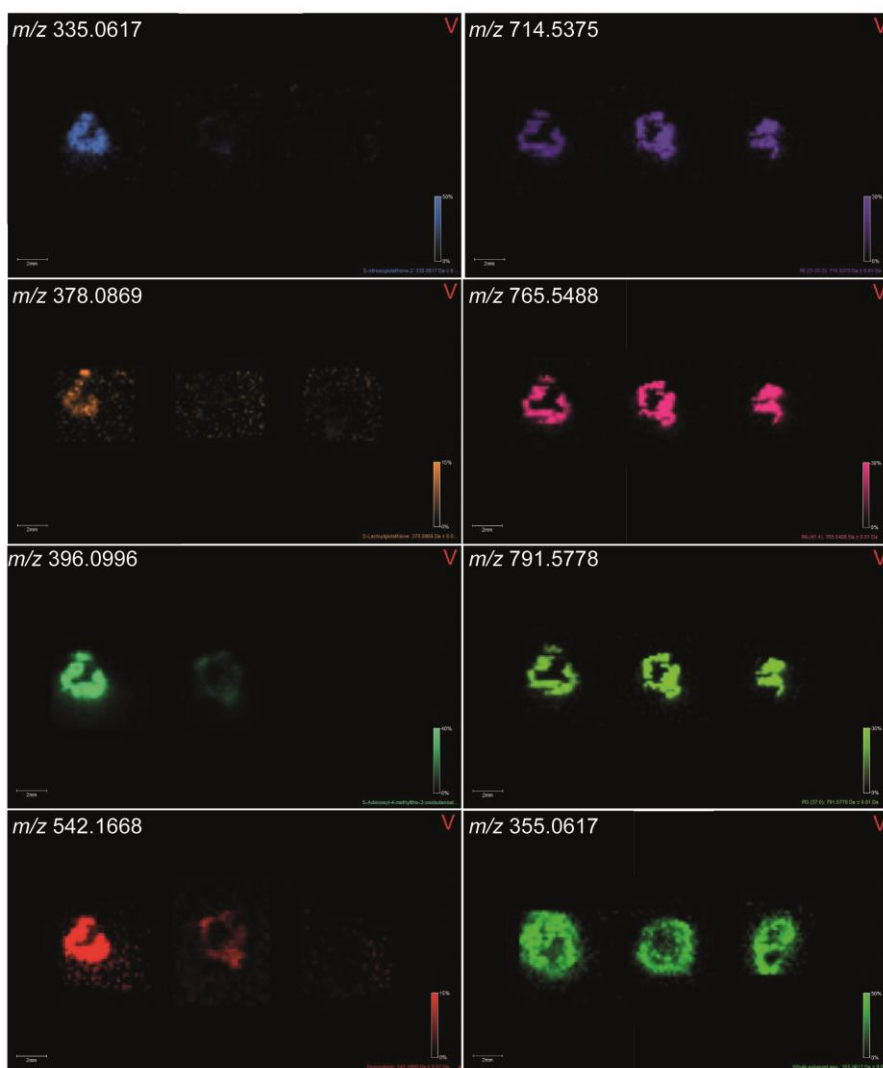
593

594 **Figure 3:** Effects of Doxorubicin on SAOS-2 cells. a) SAOS-2 cells responded to doxorubicin
 595 treatment in 2D cell culture, as determined by Resazurin assay. b) SAOS-2 did not show
 596 significant reduction in activity after treatment with Doxorubicin at doses in excess of the
 597 IC_{50} value determined from the 2D culture. c) Fluorescence microscopy of Hoechst 33342
 598 staining (blue), and Doxorubicin (red) localisation throughout aggregated spheroid,
 599 confirming drug uptake into the aggregated spheroid. Scale bar = 500 μ M. d and e)
 600 Detection of Doxorubicin in positive mode m/z 544.1827 by FT-ICMS (e), whereas this was
 601 not visible by Q-TOF (d) due to a close interfering peak. f) Detection of doxorubicin in
 602 negative mode in the cell-spiked array plug vs. ATP/APD for cellular co-localisation.
 603 Presence of Doxorubicin in a 4 μ m-treated spheroid aggregate is shown.



611
 612
 613
 614
 615
 616
 617
 618
 619
 620

Figure 5: Normalised signal intensity of six ionic peaks at 0, 0.8 and 4 μM Doxorubicin treatments. Data is from three independent batches, with three sections analysed for each experiment. Significant differences between pairs of doses from *t* tests within a linear mixed model are indicated. Fitted values for each dose from the linear mixed model are shown as horizontal lines across the data.



621

622

623 **Figure 6:** Negative mode FT-ICR MSI of selected targets altered by Doxorubicin and initially
 624 identified by PCA-DA. Treatment groups are 4 μM , 0.8 μM and control. m/z 355.0617
 625 identified the whole spheroid aggregate, and m/z 542.1668 is Doxorubicin, which shows
 626 predominant localisation in the centre of the spheroid. m/z 335.0617, m/z 378.0869 and m/z
 627 396.0996 show striking increased in response to Doxorubicin, consistent with PDA-DA
 628 analysis. The remaining species are putatively identified as lipids and show a similar spatial
 629 distribution.

630

631